Nuclear Engineering and Design 429 (2024) 113642

Contents lists available at ScienceDirect

Nuclear Engineering and Design

journal homepage: www.elsevier.com/locate/nucengdes

Toward development of a low-temperature failure envelope of cases for high-burnup RIAs under PWR operational conditions

L. Aldeia Machado [a,*], K. Nantes [a], E. Merzari [a], L. Charlot [b], A. Motta [a], W. Walters [a]

[a] Ken and Mary Alice Lindquist Department of Nuclear Engineering, Pennsylvania State University, University Park, PA 16802, United States of America
[b] Idaho National Laboratory, Idaho Falls, ID, 83415, United States of America

ARTICLE INFO

Keywords:
RIA
HIGH-BURNUP
PCMI
CHF
SOBOL sensitivity analysis

ABSTRACT

A Reactivity-Initiated Accident (RIA) is a design-basis accident that occurs when the reactor loses one of its control rods. A reactivity insertion will follow such events, drastically increasing the fuel pellet's temperature and volume due to thermal expansion. The fuel pellet and the cladding will interact mechanically, which could lead to cladding failure. This work presents the development of cases where low-temperature failures are more likely to happen for high-burnup fuels under PWR operational conditions. A coupled computational model between the nuclear fuel performance code BISON, MOOSE's Thermal-Hydraulic Module (MOOSE-THM), and MOOSE's Stochastic Tools Modules (MOOSE-STM) was created to study the thermal-hydraulic behavior of a high-burnup fuel rodlet during the first stages of an RIA transient, allowing us to identify three scenarios: the system reached CHF, leading to high-temperature failure, the system failed due to PCMI, or the system survived the whole transient without failing. To address these scenarios, we performed a sensitivity analysis with more than 140,000 model replicates through MOOSE-STM varying parameters such as the power pulse width, power pulse total energy deposition, hydride rim thickness, coolant inlet temperature, and coolant inlet mass flux. We also compared two PCMI failure criteria in our analysis. Our results suggest that the hydride rim thickness and the power pulse width will be the key parameters impacting the failure type our system would undergo during the power transient. Using the data from our simulations, we constructed two failure maps, one for each PCMI failure criterion, showing how the failure type is affected by each parameter considered in the sensitivity analysis. We also provided a closed-form expression for the boundary between the PCMI and CHF failure types as a function of the hydride rim thickness and power pulse width.

1. Introduction

Reactivity-initiated accidents (RIA) are design-basis accidents that occur when a control rod is lost due to mechanical failure in the rod control system, leading to a control rod drop in a Boiling Water Reactor (BWR) or rod ejection in a Pressurized Water Reactor (PWR) (Todreas and Kazimi, 2012). Losing a control rod will cause the fuel rod to experience a sudden increase in temperature, leading to thermal expansion and eventual interaction between the fuel pellet and the rod cladding (Boyack et al., 2001).

During an RIA, the clad can mainly fail by two different mechanisms. The first is a low-temperature failure, which happens during the first stage of the transient when the pellet quickly expands against the cladding, which is at a relatively cold temperature. Due to the lack of ductility in the clad, it can experience a catastrophic failure due to the Pellet-Clad Mechanical Interaction (PCMI) (Meyer et al., 1996; Boyack et al., 2001).

If the cladding survives this first stage, it still can fail due to the second failure mechanism, a high-temperature failure known as ballooning. In this case, the clad reaches a high enough temperature to become ductile and deform due to the extreme pellet expansion and increased fuel rod internal pressure. The cladding ballooning can be followed by clad rupture (Boyack et al., 2001).

In both cases, the clad failure can release fuel material into the coolant, leading to steam explosions that can damage the nearby fuel rods. Fragments of the fuel rod dispersed in the coolant and traveling at high speeds inside the pressure vessel can also damage the core structure.

One of the key parameters for the fuel rod failure during an RIA is the occurrence of the Departure from Nucleate Boiling (DNB) that occurs at the Critical Heat Flux (CHF). Once our system reaches the CHF, the fuel rod's ability to remove heat will decrease severely due

* Corresponding author.
E-mail addresses: lca5209@psu.edu (L. Aldeia Machado), krn5198@psu.edu (K. Nantes), ebm5351@psu.edu (E. Merzari), lise.charlot@inl.gov (L. Charlot), atm2@psu.edu (A. Motta), wjw24@psu.edu (W. Walters).

https://doi.org/10.1016/j.nucengdes.2024.113642
Received 16 April 2024; Received in revised form 11 September 2024; Accepted 9 October 2024
Available online 30 October 2024

to the formation of a thin vapor film around the rod, leading to an abrupt temperature rise in the fuel and cladding (Todreas and Kazimi, 2012). After the DNB starts, the clad will no longer be able to suffer a low-temperature failure, failing due to ballooning instead.

Another important factor in determining how the fuel rod will fail during the power transient is the capacity of the cladding to survive the first stages of the RIA without suffering a brittle failure due to PCMI, especially for high-burnup fuels. Experiments at the CABRI and NSRR reactors showed that the ability of the cladding to survive such transients markedly decreases with the exposition to radiation damage, corrosion, hydriding, and progressive bonding of the fuel and cladding, factors that are enhanced as the burnup level increases (Meyer et al., 1996; Papin et al., 2007; Beyer and Geelhood, 2013).

A series of tests assessed the fuel rod behavior during RIAs. Unfortunately, many of these results are restricted to members of the collaborations that performed these experiments, making public data about such phenomena scarce. Papin et al. (1996) present a deeper description of the initial tests performed by the CABRI REP-Na Program and their results. The REP-Na program is a well-documented and publicly available database for high-burnup RIA transients. It consists of a series of RIA tests conducted for burnup levels ranging from 33 MWd/KgU to 64 MWd/KgU where factors such as the corrosion level, fuel type, and power pulse width and amplitude were considered. The CABRI REP-Na program used liquid sodium as the coolant during the RIA tests.

By comparing the behavior of the fresh and irradiated fuel under RIA conditions, Papin et al. (1996) concluded that the irradiated fuel has a higher potential to swell during rapid heating conditions due to the accumulation of fission gas within the fuel due to the high burnup and that the embrittlement caused by the hydrogen build-up within the clad and local hydride concentrations can lead to degradation of the clad mechanical properties, leading to an early failure during the RIA transient. Papin et al. (2007) presents a complete summary of the 12 Rep-Na tests performed at the CABRI facility.

Fuketa et al. (1996) described and analyzed the RIA tests performed at Japan's Nuclear Safety Research Reactor (NSRR). These tests covered fuels with burnups ranging from 38.9 to 50.4 MWd/kgU. Stagnant water at atmospheric pressure and ambient temperature was used as the coolant during the tests. The experiment was composed of 42 tests, of which 20 used fuel irradiated in commercial reactors and had initial enrichment ranging from 2.6 to 3.4%, while the others were preirradiated at the Japan Materials Testing Reactor (JMTR) with an initial enrichment ranging from 10 to 20%.

Of the 42 tests performed by the NSRR, eight failed due to PCMI, two of which were high-burnup PWR fuel irradiated in commercial reactors, and the other six belong to the group of fuels preirradiated at the JMTR, where the high initial enrichment led to higher energy deposition levels. None of the 42 tests performed by the NSRR presented any indication of DNB. The results from these tests corroborate the suggestion presented by Papin et al. (1996) that increasing the burnup level would decrease the PCMI failure threshold. They suggested that the presence of a preexisting hydride layer within the cladding for the high had an important contribution to the rod's failure, with small cracks in the oxide and hydride layers being observed in the high-burnup tests, which can act as precursors of clad failure (Fuketa et al., 1996).

Schmitz and Papin (1999) expands the previous results by suggesting that the increased fission gas release and high pressures caused by the increased burnup may contribute to rod ballooning and rupture for the rods that reach CHF during the RIA. They also state that since the experiments used to build their database were conducted with sodium as the coolant, like the REP-Na test series, or under low temperature and pressure conditions, like the NSRR test series, where CHF is not easily reached, they do not provide the representative necessary to study the whole phenomenology behind the RIA transients, since they are not accounting for the high-temperature failure mechanisms that may occur if the clad survives the RIA first stages. They state that experimental setups capable of reproducing PWR conditions are necessary to study the phenomenology of the RIA second phase where the high-temperature failures happen.

Biard et al. (2020) describes the modifications implemented on the CABRI facility to address the necessity to provide representative conditions for Light Water Reactors (LWR) fuel types. In particular, the sodium loops were dismantled and replaced by water loops capable of reaching PWR operational conditions regarding temperature, pressure, and flow rate. Papin et al. (2006) presented the results of the CIP reference tests performed in 2002 before the water loop replaced the sodium loop. These tests comprise two fuel rods with advanced cladding: EDF-AREVA M5^{TM} clad and A06-ENUSA Zirlo® clad, irradiated up to 75 MWd/kgU and subject to power pulses with widths around 30 ms half-width and maximum energy deposited of 90 and 99 cal/g respectively. Results from the tests showed that both rods survived the power transient. The authors also underlined that for cases with high corrosion levels, the risk of PCMI will increase for faster power pulses (10 ms) with higher energy deposition (> 110 cal/g) for PWR conditions.

In the United States, high-burnup fuel RIA experiments are being conducted at the Idaho National Laboratory (INL) Transient REActor Test (TREAT). Kamerman et al. (2022) describes the experimental setup utilized for the INL team in conducting the High-burnup Experiments in Reactivity Initiated Accidents (HERA) tests. TREAT experiments are currently conducted in a static water capsule capable of reproducing an LWR environment. The power pulse width for the HERA tests performed at the TREAT facility will range from 50 to 600 ms. For these tests, the radial peak enthalpy must be sufficient to ensure rod failure, which can happen due to PCMI or ballooning.

The CABRI and NSRR tests provided data used to validate the most commonly used nuclear materials codes. Parallel to the conduction of the REP-Na series tests, the Insitute for Protection and Nuclear Safety (IPSN - *l'Institut de Protection et de Sûreté Nucléaire*) developed the SCANAIR code to predict the fuel-rod behavior during RIA transients based on the data from the REP-Na series experiments (Papin et al., 1996). REP-Na data was also used by the Electric Power Research Institute (EPRI) to validate their Nuclear Fuel Performance Code FALCON (EPRI, 2004). NSRR FK and REP-Na experimental data were used to validate BISON, INL's Nuclear Materials code, Folsom et al. (2017).

Efforts are also being conducted to understand better the physical mechanisms behind the second phase of RIAs, particularly the system's thermal-hydraulic response during the power transient. Hernandez et al. (2022) performed a Sobol sensitivity analysis to quantify the impact of Heat Transfer Time Constante (HTTC), Heat Transfer Coefficients (HTC) multipliers, such as natural convection, nucleate, transition, and film boiling multipliers, as well as the CHF multiplier for two selected TREAT experiments. A gap thickness factor was also considered during the Sobol analysis to quantify the fuel expansion during the transient. Their results indicate that the CHF factor has the biggest impact on the peak cladding outer temperature and the second most significant impact on the DNB time-of-occurrence, following the gap thickness factor. The HTTC presented a high impact on the peak cladding outer temperature under DNB conditions, as well as the DNB time-of-occurrence.

Seo et al. (2021) also performed a sensitivity analysis over the TREAT facility pool boiling CHF experiment designs, focusing on the power transient impact over the system thermal-hydraulic behavior. Their results suggest that the total energy deposition into the system dominates the cladding inner and outer surface temperatures once the system reaches CHF. If the system does not reach CHF, the coolant subcooling level will dictate the clad outer temperature distribution. They also performed a Sobol analysis accounting for the system power-pulse history. Their results indicate that the power pulse Full Width at Half Maximum (FWHM) contributed most significantly to the clad inner and outer surface temperatures, indicating that the energy deposition

rate is more dominant than the total energy deposition in determining the clad temperature. Overall, the total energy deposition had the most relevant impact on the fuel behavior during the transient, with the CHF occurrence impacting the fuel's thermal-hydraulic behavior.

In this work, we will focus on developing an envelope of cases where low-temperature failures are more probable during RIAs for PWR conditions and high-burnup fuels, addressing the necessity of performing the tests with the representativity necessary to study the phenomenology behind the RIA transients highlighted by Schmitz and Papin (1999). Our computational model comprised a coupled system between the nuclear materials code BISON (Williamson et al., 2021), the Multiphysics Object-Oriented Simulation Environment (MOOSE) thermal-hydraulic module MOOSE-THM (Hansel et al., 2024), and MOOSE's Stochastic Tools Module (MOOSE-STM) (Slaughter et al., 2023). In this context, BISON will solve the temperature distribution over the fuel rod, transferring the rod's outer wall temperature to MOOSE-THM, where a one-dimensional, single-phase flow channel model will perform the thermal-hydraulics calculations and transfer back to BISON the bulk coolant temperature and the convective heat transfer coefficient. BISON will then use these values on a convective boundary condition applied to the rod's outer wall, updating the fuel rod temperature and starting the transfer process again. To handle some of the complexity involving modeling an RIA transient, we implemented a series of correlations into MOOSE-THM to account for phenomena such as the subcooled flow boiling and the critical heat flux. We also implemented a new correlation for the PCMI failure criterion into BISON based on the hydride rim thickness.

Based on the results of Schmitz and Papin (1999), Boyack et al. (2001), and Seo et al. (2021), we considered in our Sobol sensitivity analysis the power pulse amplitude and FWHM, as well as the hydride concentration within the clad before the power transient as our input parameters. We acquired the Sobol indices for the failure type (CHF, PCMI, or No Failure) and physical quantities as the pellet-cladding contact pressure, fuel temperature, and hoop strain.

2. Methods

This section presents the methodology used in this work. We will start by introducing the governing equation used by BISON and MOOSE-THM. Afterward, we will show the computational model geometry, mesh, and boundary conditions. We will also introduce the set of correlations implemented in MOOSE-THM to better represent the physics of our problem. The computational model section will also describe the Sobol sensitivity analysis parameters. Following the computational model, a description of the three models used to analyze BISON neutronics capability is presented.

2.1. BISON governing equations

BISON is a finite element-based nuclear fuel performance code capable of solving fully-coupled thermomechanical problems, containing the necessary multiphysics to solve RIA transients simulations (Williamson et al., 2021). As part of the MOOSE framework, BISON can be directly coupled with other MOOSE-based codes, allowing us to model multi-physics and multi-scale problems. BISON governing equations comprise fully coupled partial differential equations for energy, species, and momentum conservation (Hales et al., 2015).

The energy balance is given by:

$$\rho C_p \frac{\partial T}{\partial t} + \nabla \cdot \mathbf{q}'' - e_f \dot{F} = 0, \tag{1}$$

where T is the temperature, ρ and C_p are, respectively, the density and specific heat. $\dot{F}$ is the volumetric fission rate and e_f is the energy released per fission event. The heat flux will be given by:

$$\mathbf{q}'' = -k\nabla T, \tag{2}$$

where k is the thermal conductivity.

2.2. MOOSE Thermal-Hydraulic Module (MOOSE-THM) governing equations

MOOSE-THM is an open-source code and part of the MOOSE framework that can create single-phase, variable area, inviscid, and compressive flow models. In our model, it will be used to replace BISON's coolant channel object. MOOSE-THM offers us more flexibility in the implementation of new correlations that are not present in BISON, such as Groeneveld's CHF lookup tables (Groeneveld et al., 2007). MOOSE-THM also allows us to add thermal-hydraulics parameters to our sensitivity analysis. MOOSE-THM treats the flow components as one-dimensional with a variable cross-sectional area that varies along the axial direction (Hansel et al., 2024). For a single-phase flow, MOOSE-THM will use the following area-averaged balance equations, assuming that the covariance terms of the averaging process are negligible (Berry et al., 2014):

$$\frac{\partial}{\partial t} A\langle \rho \rangle_A + \frac{\partial}{\partial x} A\langle \rho U \rangle_A = 0, \tag{3}$$

for the mass balance, where $U = \mathbf{U} \cdot \hat{\mathbf{n}}_{\mathbf{x}}$ is the component of velocity in the flow direction.

$$\frac{\partial}{\partial t} A\langle \rho U \rangle_A + \frac{\partial}{\partial x} A(\langle \rho U^2 \rangle_A + \langle p \rangle_A) = -\tilde{p}\frac{\partial A}{\partial x} - F_{friction}, \tag{4}$$

for the momentum, where $\tilde{p}$ is the average pressure around the perimeter of the duct cross-section, and $F_{friction}$ is the average wall shear stress. For the total energy we have:

$$\frac{\partial}{\partial t} A\langle \rho E \rangle_A + \frac{\partial}{\partial x} A(\langle \rho E \rangle_A + \langle pU \rangle_A) = -\tilde{p}\frac{\partial A}{\partial t} + Q_{wall}, \tag{5}$$

where $E = e + \frac{\mathbf{UU}}{2}$ is the specific total energy, e is the specific internal energy, Q_{wall} is the average heat transfer rate between from the duct wall to the fluid.

2.3. Computational model

Our computational model aims to replicate the setup of one of the RIA tests performed at the CABRI facility, specifically the REP-Na3 test. These tests used a liquid sodium loop to reproduce the PWR coolant operational conditions (Papin et al., 1996, 2006, 2007). However, using sodium as a coolant disregards the occurrence of high-temperature phenomena such as CHF.

The model itself consists of three coupled applications, each of which is responsible for a different aspect of our problem. BISON will evaluate the fuel rod response to variations in the reactor power, MOOSE-THM will resolve the thermal-hydraulic response to these variations, and MOOSE-STM will be responsible for sampling the cases and input parameters used for the Sobol sensitivity analysis.

2.3.1. BISON computational model

BISON is responsible for solving the fuel rod response during the irradiation process and RIA, resolving the temperature distribution, thermal expansion, and pellet-clad mechanical interaction. Our model is composed of a UO2 fuel rodlet with a Zircaloy-4 cladding and an initial enrichment of 4.5 at.%. The rodlet was refabricated from a fuel rod that was irradiated inside a commercial PWR to increase its burnup level, as described by Papin et al. (1996, 2006, 2007).

We used the NFIR (Nuclear Fuel Industry Research) correlation (Marion, 2006) for the fuel thermal conductivity. The fission gas release was modeled using the Simple SIFGRS (Simple Integrated Fission Gas Release and Swelling) model, which incorporates the fundamental features of fission gas behavior (Hales et al., 2015). The MOOSE Solid Mechanics Module was used as the mechanical model. The pellet-cladding contact was modeled using the MORTAR formulation. Which is more suitable to perform PCMI modeling since it prevents artificial spacial interface variable oscillations from happening, a common problem seen in node-on-face contact models (Recuero et al., 2022). This configuration was used in both steps of our model: the irritation

Table 1
Geometric parameters for the BISON REP-Na3 model.

Pellet radius [cm]	Clad inner radius [cm]	Clad outer radius [cm]	Fuel length [cm]
$\mathbf{R_{fo}}$ 0.40956	$\mathbf{R_{ci}}$ 0.41776	$\mathbf{R_{co}}$ 0.47736	$\mathbf{h_f}$ 43.4848
Bottom gap [cm]	Top gap [cm]	Pellet-Clad gap [cm]	Rodlet Length [cm]
δ_{bot} 0.3	δ_{top} 2.98168	δ_{gap} 0.082	$\mathbf{h_r}$ 47.0664

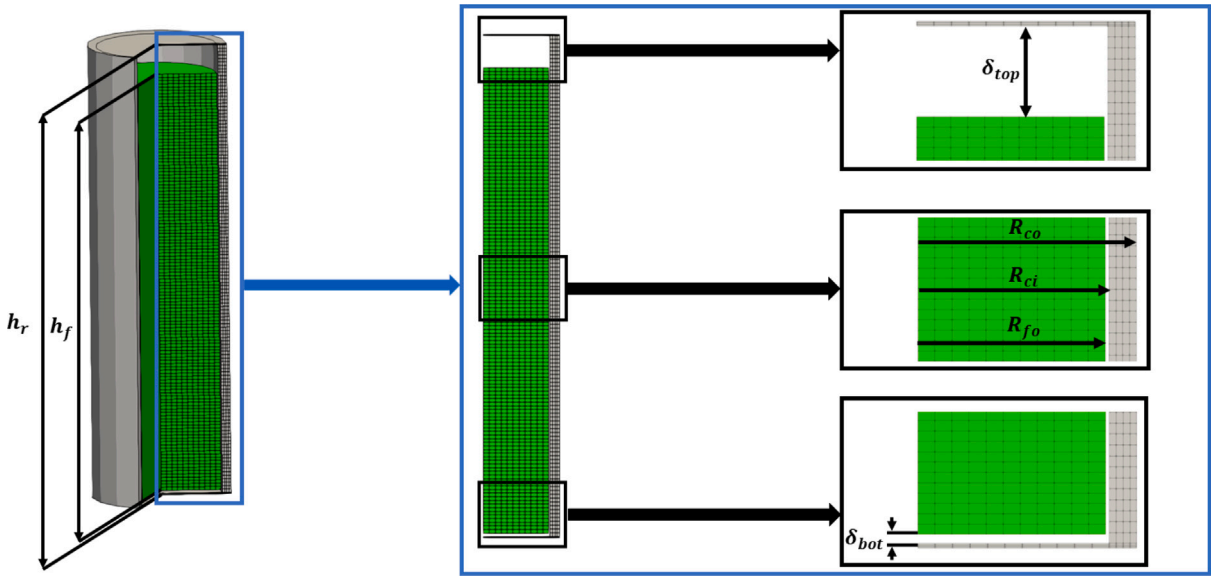

Fig. 1. REP-Na3 BISON model geometry.

and the RIA steps, with the difference that for the irradiation step, initial conditions are provided by the user, while for the RIA transient simulation, the initial conditions are given by the final state of the irradiation step model.

Fig. 1 shows the fuel rodlet geometry. We used an axisymmetric smeared mesh to represent these regions (Hales et al., 2015). Our mesh comprises 11 nodes in the pellet radial direction and 128 in the axial direction. For the cladding, these values are, respectively, 4 and 130. Table 1 shows the geometric parameters used to construct the model geometry.

As boundary conditions, we fixed the cladding and fuel bottom displacements as zero. At the fuel centerline, the temperature must be finite, and no displacement in the negative radial direction was allowed. At the outer cladding surface, the heat flux follows Newton's law of cooling, given by:

$$\left|\mathbf{q}''(z)\right| = h_{cool}(z)\left[T_{wall}(z) - T_{cool}(z)\right], \tag{6}$$

where T_{wall} is the wall temperature. The coolant convective heat transfer coefficient, h_{cool}, and the coolant temperature, T_{cool}, are solved in MOOSE-THM.

Before undergoing the power transient, the fuel rod used during this CABRI REP-Na3 test was irradiated in a commercial PWR up to a burnup level of around 53.8 MWd/kgU. Fig. 2 (left) shows us the power history used to irradiate the fuel rod. After reaching the desirable burnup, the fuel rod was refabricated into the rodlet used in the experiment, which was performed in a liquid sodium loop system. It is worth to mention that MOOSE-THM was also used as the thermal-hydraulic solver during the irradiation step. For the REP-Na3 test, the irradiated fuel was exposed to a Gaussian power pulse with an FWHM of 9.5 ms, depositing 122 cal/g into the fuel (Papin et al., 2007). For our model, the linear heat rate during the RIA was modeled as a normalized Gaussian pulse, given by:

$$q'(z,t) = \left(\frac{E_d.M}{h_f.c}\right)\frac{1}{\sqrt{2\pi}\sigma}\exp\left[-\frac{1}{2}\frac{(t-t_0)^2}{\sigma^2}\right]P_f(z) \tag{7}$$

where

$$\sigma = \frac{\text{FWHM}}{2\sqrt{2ln2}}, \tag{8}$$

dictates the power pulse width, t_0 is the location, in seconds, of the pulse maximum, E_d, in cal/g, is the power pulse total energy deposition, M is the fuel mass, in kilograms, h_f is the fuel length, in meters, $c = 0.0002388459$ is a conversion factor from cal/g to J/kg, and $P(z)$ is the power axial peaking factor. Fig. 2 (right) shows some of the Gaussian power pulses used during our analysis. The quantity Time* is equal to the difference between the current time and the final time for the irradiation process in seconds and was chosen to simplify the power pulse visualization when plotted as a function of the time.

BISON has implemented a Zircaloy-4 failure criteria due to PCMI under RIA conditions. This failure criterion is a function of the peak radial average enthalpy increase on the fuel and the average hydrogen content as hydride in the cladding. The increase in the average radial enthalpy that leads to failure is given by (Hales et al., 2015; Clifford, 2020):

$$\Delta H_{fail} = \begin{cases} \min\left[150, (1.6*10^5)C_{prec}^{-1.5} + 45\right], & \text{for } T_0 \le 533.15\ [K] \\ \min\left[150, (1.8*10^5)C_{prec}^{-1.5} + 60\right], & \text{for } T_0 > 533.15\ [K] \end{cases} \tag{9}$$

where ΔH_{fail} is given in cal/g, C_{prec} is the total hydride content in the cladding in ppm, and T_0 is the clad temperature before the start of the transient.

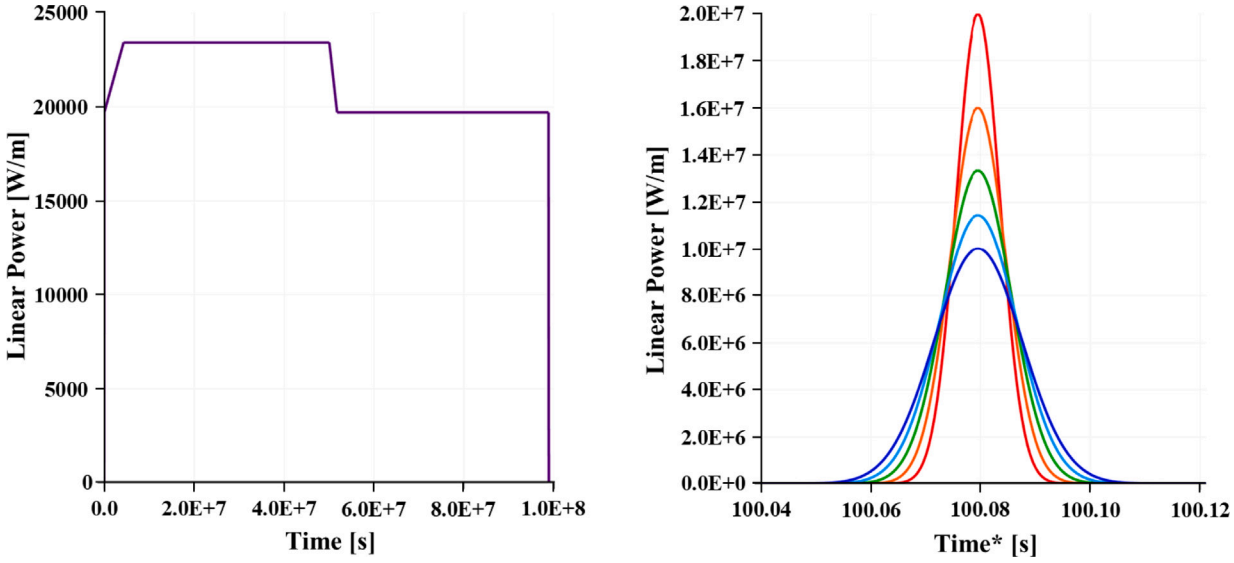

Fig. 2. Power history for the irradiation process (left) and for the RIA transient (right) as a function of time.

It is well understood that the PCMI cladding failure depends strongly on the hydrogen localization that happens due to temperature gradients, to which the cladding is exposed during the in-reactor time, as it decreases the cladding overall ductility (Nantes et al., 2024b). Therefore, the simple approximation of the current criteria, considering only the average hydride distribution, seems inappropriate for a good estimation of cladding failure probability. To address this issue, Nantes et al. (2024a) developed a model to predict cladding failure by considering the possibility of a hydride rim formation. This model is based on experimental work (Daum, 2007; Bates, 1998; Link, 1997) and estimates the failure strain as:

$$\epsilon_{failure} = 0.06332 - 2.5498 \times 10^{-4} \delta_{Rim} \tag{10}$$

where δ_{Rim} is the hydride rim thickness in μm. The hydride rim thickness is related to the radial average hydride concentration through (Nantes et al., 2024a):

$$\delta_{Rim} = \frac{\overline{C_{prec}}}{2700} \left(\delta_{clad} - \delta_{oxide}\right) * 10^6 \tag{11}$$

where δ_{clad} is the cladding thickness, δ_{oxide} is the oxide thickness, and C_{prec} is the radial average hydride concentration. For simplicity, we disregarded the influence of the oxide thickness in this conversion. We also assumed that the hydride rim would be constant over the axial direction, implying that the radial average hydride concentration is the same as the average hydride concentration.

2.3.2. MOOSE Thermal-Hydraulic Module (MOOSE-THM) computational model

MOOSE-THM geometry consists of a one-dimensional channel that shares the same number of elements and nodes with the clad outer surface, respectively 130 and 131. For a wall temperature given by BISON, MOOSE-THM will compute the convective heat transfer coefficient and coolant temperature. These values will be transferred to BISON to solve the convective boundary condition, Eq. (6), in the outer clad surface. The REP-Na3 test was realized with sodium as a coolant. The inlet temperature and mass flux were fixed as 553.15 K and 3533 $kg/m^2 \cdot s$ to approximate the sodium loop condition to the operational conditions of a pressurized water reactor. The pressure at the channel outlet ranged from 0.1 to 0.5 MPa during the test. For the liquid sodium convective heat transfer coefficient, we implemented the Schad correlation into MOOSE-THM (Todreas and Kazimi, 2012):

$$\begin{aligned} Nu_{Schad} &= 4.496 \left[-16.15 + 24.96\left(\frac{P}{D}\right) - 8.55\left(\frac{P}{D}\right)^2\right] \cdot \left(\frac{Pe}{150}\right)^{0.3}, \\ h_{Schad} &= \frac{Nu_{Schad}.k}{D_h} \end{aligned} \tag{12}$$

Eq. (12) is valid for a pitch-to-diameter ratio, P/D, between 1.1 and 1.4 and a Peclet number, Pe, between 150 and 1000.

Currently, MOOSE-THM does not have liquid sodium properties implemented on it. To run the coupled model using sodium as a coolant, we used MOOSE-THM's stiffened gas fluid properties model (Métayer et al., 2004) to reproduce the liquid sodium density and enthalpy as a function of temperature. The heat capacity, thermal conductivity, and viscosity were considered constants. The stiffened equations of state for the density and enthalpy are:

$$\rho(p,T) = \frac{p + p_\infty}{(\gamma - 1) C_V T}, \tag{13}$$

$$H(T) = \gamma C_V T + q, \tag{14}$$

where p is the pressure, C_V is the heat capacity at constant volume, $\gamma = C_P/C_V$ is the ratio of specific heat capacities. The constants $q = -279,991.5318$ and $p_\infty = 90,367,775.1282$ were adjusted to approximate the liquid sodium density and enthalpy as a function of the temperature for a pressure equal to 0.5 MPa.

To use water as the coolant, we assumed an interior subchannel and varied the pitch-to-diameter ratio, P/D, from 1.1 to 1.4, the mass flux, G, from 3000 to 4000 $kg/m^2 \cdot s$, and the subchannel inlet temperature, T_{inlet}, from 563 to 598 K, covering a broad range of PWRs operational conditions. We defined the coolant outlet pressure as constant and equal to 15.55 MPa. For the friction factor, we used the Cheng and Todreas correlation, Todreas and Kazimi (2012):

$$f = \frac{1}{Re^{0.18}} \left[0.1339 + 0.09059\left(\frac{P}{D} - 1\right) - 0.09926\left(\frac{P}{D} - 1\right)^2\right]. \tag{15}$$

For a subcooled flow in a rod bundle, the Nusselt can be given by the Weisman correlation (Todreas and Kazimi, 2012):

$$Nu_{Weis} = 0.023 \left[1.826\left(\frac{P}{D}\right) - 0.2609\right] Re^{0.8} Pr^{0.4}, \quad h_{Weis} = \frac{Nu_{Weis}.k}{D_h} \tag{16}$$

Table 2
Eq. (19) coefficients.

G [kg/m^2.s]	a	b	c	d	e	f
3000	2.775401733	−9.087833331	6.30346114	8.548559446	−12.15868427	3.580103449
3500	2.86833576	−9.320196877	7.06681586	7.892435413	−13.01091906	4.46962673
4000	3.031742144	−9.381271294	7.66041102	7.089838238	−14.73962158	6.325693343

for $0.7 < Pr < 100$. The Prandtl, Pr, and Reynolds, Re, numbers are giver by:

$$Pr = \frac{C_p \mu}{k}, \quad Re = \frac{G D_h}{\mu}, \tag{17}$$

where G is the mass flux, μ the viscosity, and D_h the subchannel hydraulic diameter.

The coolant will experience nucleation near the rod walls as the wall temperature rises, even though the coolant bulk temperature is below saturation. This phenomenon is known as subcooled boiling. For a subcooled flow boiling regime, we can use Thom's correlation to determine our heat transfer coefficient (Todreas and Kazimi, 2012):

$$T_{w,Thom} = T_{sat} + 22.7 \left[\frac{q''}{exp(2.p/8.7)} \right]^{0.5}, \quad h_{Thom} = \frac{q''}{T_{w,Thom} - T_m}, \tag{18}$$

where q'' is the wall heat flux in megawatts per square-meter, p is the pressure in megapascal, T_{sat} is the saturation temperature, and T_m is the coolant bulk temperature. If the heat flux keeps rising, we will eventually reach the Critical Heat Flux (CHF), where a phase change occurs in the coolant near the fuel rod wall, forming a film of steam near the wall, dramatically reducing the heat transfer efficiency of our system.

The critical heat flux is a key parameter during RIA transients. Once we reach the CHF, the clad temperature will increase quickly, the alloy that composes the clad will become malleable, and the hydrides will be diluted, making a low-temperature catastrophic failure impossible. Dozens of correlations are available to predict the occurrence of CHF. For a given mass flux and pressure, we can determine the CHF as a function of the equilibrium quality using Groeneveld's lookup tables (Groeneveld et al., 2007). For the pressure and mass flux range of our system, the CHF as a function of the equilibrium quality will be given by:

$$\begin{aligned} &q''_{CHF/Table}(Xe) \\ &= \left(a + b * Xe + c * Xe^2 + d * Xe^3 + e * Xe^4 + f * Xe^5\right) * 10^6, \end{aligned} \tag{19}$$

where the equilibrium quality is given by:

$$Xe = \frac{H(T) - H_f}{H_g - H_f}, \tag{20}$$

and H is the coolant enthalpy as a function of the temperature, H_f is the coolant saturation enthalpy for the liquid, and H_g is the coolant saturation enthalpy for the gas. Our model is limited to subcooled conditions since MOOSE-THM can only solve single-phase problems. This limits our capacity to simulate post-CHF phenomena such as film boiling. To avoid extrapolating MOOSE-THM limitations, we terminate our simulation when the wall heat flux is greater or equal to the critical heat flux, ensuring that we stay in a flow regime with $X_e \leq 0$. The coefficients in Eq. (19) are presented in Table 2.

Other critical heat flux values inside this range of mass fluxes can be obtained through the linear interpolation of the values obtained through Eq. (19). The Groeneveld's lookup tables were developed for a circular tube with 8 mm diameter, and to be used in different geometries, it must be adjusted by a correction factor. For rod bundles (Groeneveld, 2019) recommend the use of:

$$q''_{CHF/Bundle}(Xe) = \left(\frac{D_h}{0.008} \right)^{0.5} q''_{CHF/Table}(Xe) \tag{21}$$

2.3.3. MOOSE stochastic tools module (MOOSE-STM) computational model

MOOSE-STM was responsible for sampling the uncertainty values and controlling each model evaluation performed during the sensitivity analysis. Since we are interested in mapping the condition that may enhance the chances of our system undergoing a low-temperature PCMI failure, we choose to consider the following quantities in our sensitivity analysis: the power pulse total energy deposition, the power pulse FWHM, the hydride rim thickness, the pitch-to-diameter ratio, the coolant mass flux and inlet temperature. We uniformly sample these quantities within their range to cover a broader range of operational conditions.

We used the batch-reset mode option on MOOSE-STM to reduce the total running time to evaluate all the replicates and perform the statistical analysis. This allows us to create one sub-application for each processor we are using to run the model and initialize it for each sample (Slaughter et al., 2023). For this analysis, we performed 100,800 model evaluations divided into 18 simulations, each performing 5600 model evaluations. We combined the outputs of these simulations through a Python script before calculating the Sobol indices. Fig. 3 shows the outer loop workflow for our coupled model, which is performed for each model evaluation. Fig. 4 shows the inner loop of our coupled model where the MOOSE-THM/BISON coupled model is used to determine our system failure type. This inner loop is performed for each timestep of each model evaluation.

3. MOOSE-THM/BISON REP-Na3 model verification and validation

For the MOOSE-THM/BISON Rep-Na3 coupled model validation, we use some of the REP-Na tests available data (Papin et al., 1996, 2006, 2007). Fig. 5 compares our coupled model, the REP-Na3 coolant temperature measures for the first second after the power transient begins, and the SCANAIR model results assuming a closed gap and no oxide spalling (Papin et al., 2007). The experimental data presented were collected through thermocouples positioned at different azimuthal locations at the Top of the Fissile Collum (TFC) near the rodlet outlet.

It is worth mentioning that the gap between the cladding and fuel will be closed for high burnup fuels, with bonding between the fuel and the inner layers of our cladding. These factors will highly impact the gap conductance and are absent in our model. Our systems start with an open gap that closes as the fuel temperature rises, increasing the gap conductance in the process. This may explain the divergence in the experimental and computational temperature profiles. Another factor that may impact the coolant temperature distribution is our approximation of the sodium fluid properties as a stiffened gas. Table 3 also compares the experimental and computational models. Overall, we have a good agreement between the computational and experimental models. However, the maximum hoop strain presented a relative difference of 45% between the models, which we also believe to be related to the pellet-cladding gap not being closed during the beginning of the transient.

We also compared against experimental data and performed a code-to-code benchmarking between our coupled model and a BISON standalone model, where its native coolant channel solver was used to model the coolant behavior during the RIA. Fig. 6 (left) shows the fuel rod radial temperature distribution at Z = 0.22 meters for both models at different times after the beginning of the power transient. Fig. 6 (right) presents the average temperature temporal evolution for

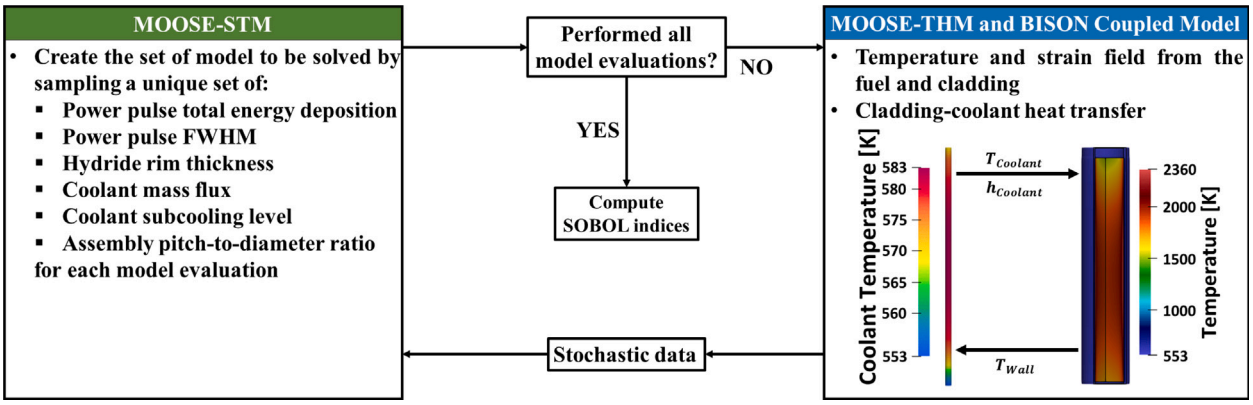

Fig. 3. Coupled model outer loop workflow.

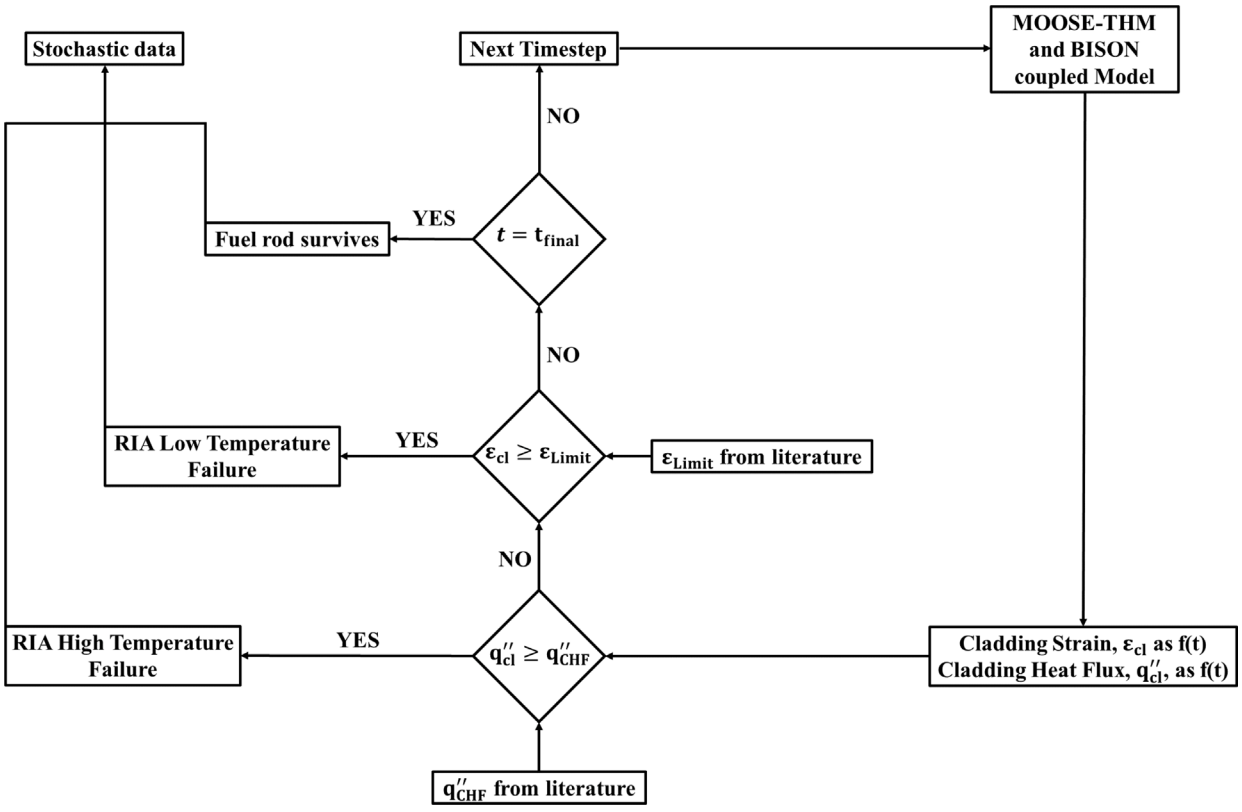

Fig. 4. Coupled model inner loop workflow.

Table 3
REP-Na3 computational model validation.

Model	Computational	Experimental	Relative error [%]
Energy deposition [cal/g]	112.56	122	7.737704918
Peak fuel enthaly [cal/g]	139.43	124	12.44354839
Max. Hoop strain [%]	1.2	2.2	45.45454545
Max. TFC temperature [K]	720.954	709.15	1.664527956

different components for both models during the first second after the RIA begins. Fig. 6 also highlights the good agreement between these two models concerning the temperature distribution within the solid domain of our problem.

Verification tests were performed to assess MOOSE-THM's capabilities to perform problems using water as a coolant. However, the difficulty in accessing data for RIA transients using water as a coolant makes it difficult to validate our coupled model for this configuration.

4. Results

This section comprises the work results, starting with the MOOSE-THM/BISON coupled model using water as a coolant during the RIA transient for PWRs operational conditions. Afterward, we present the results of our sensitivity analysis and a comparison between the two criteria used to determine if we faced a PCMI failure.

4.1. BISON and MOOSE-THM RIA coupled model under PWR operational conditions

Due to the high thermal conductivity of liquid metals, the REP-Na program underestimates the temperature distribution in the fuel rod by using sodium as a coolant. In a pressurized water reactor, the water near the rod walls will experience a phase transition driven by the high temperatures in the clad outer surface during the power transient. This

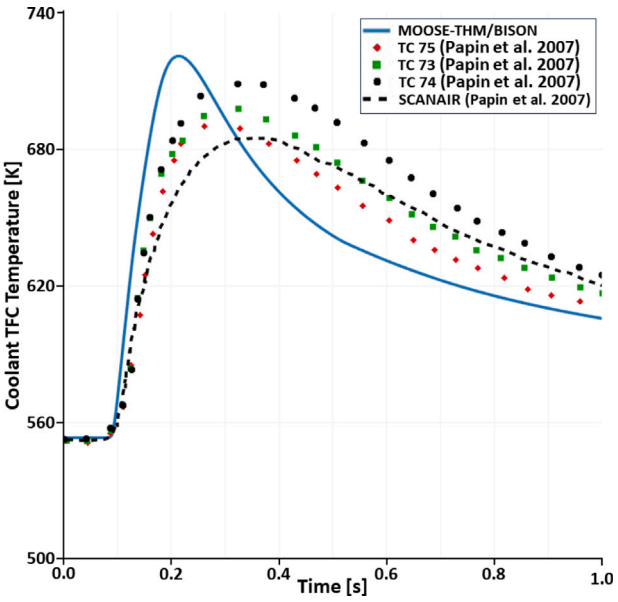

Fig. 5. Coolant temperature validation for the TFC.

phase transition will happen even if the coolant bulk temperature is smaller than the saturation temperature in a phenomenon known as subcooled boiling. If not controlled, the subcooled boiling regime will evolve into a film boiling regime, leading to a violent increase in the clad temperature (Todreas and Kazimi, 2012).

Fig. 7 shows the temperature distribution over the fuel rod when we reach the critical heat flux for the coupled model with a pulse width of 9.5 [ms] and water as coolant. There, we can see that, in the fuel, the maximum temperatures occur near the fuel surface. Such behavior is expected due to the burnup rim structure formed during irradiation. This region is rich in plutonium 239, which increases the energy deposition in the outer areas of the fuel.

The CHF prediction was realized in MOOSE-THM by comparing the wall heat flux, given by Eq. (6), with the expected critical heat flux from the Groeneveld lookup tables, Eq. (21). We present the outer wall temperature, heat flux, and critical heat flux as a function of the axial position in Fig. 8.

The wall temperature presents a slightly parabolical distribution for the subcooled flow regime. Once we reach the subcooled boiling flow regime, the phase transition and the turbulence caused by the boiling will increase the convective heat transfer coefficient, slowly increasing the wall temperature. Due to the increase in heat conductance, the heat flux in the wall will also rise. The coolant bulk temperature will increase, increasing the coolant equilibrium quality and reducing the heat flux necessary to reach the film boiling (Todreas and Kazimi, 2012). We terminate the simulation immediately once the wall heat flux surpasses the critical heat flux.

4.2. Pellet-cladding mechanical interaction failure map

Fig. 9 shows the type of failure our system would suffer during the RIA transient as a function of the pulse total energy deposition, E_d, pulse FWHM, the hydride rim thickness, δ_{Rim}, the pitch-to-diameter ratio, P/D, and the coolant mass flux, G, and inlet temperature T_{inlet} for the strain based PCMI failure criterion. Each dot on Fig. 9 represents one of the 100,800 model evaluations we performed during our sensitivity analysis, with around 8.16% of our cases failing due to PCMI.

Our results suggest that the hydride rim thickness and the pulse width will be the main factors impacting the type of failure our system will undergo during the RIA. Thicker hydride rim structures within the cladding act in favor of PCMI failures by decreasing the strain necessary to cause a brittle failure. This behavior is clearly represented in 9, where we can see that the distribution of cases that suffered PCMI failures is concentrated in the regions with thicker rims. The second most notable correlation between uncertainty and our system failure type is the pulse width, where we can see that narrow pulses will favor the PCMI occurrence. This behavior can be explained by the fact that wider pulses will cause the energy to be slowly deposited within our system, which will provide enough time for our cladding and coolant temperature to rise, which will act in favor of a CHF failure. This phenomenon can be seen in Fig. 10(c), where the cases with a larger pulse undergo a PCMI failure at a much higher average cladding outer

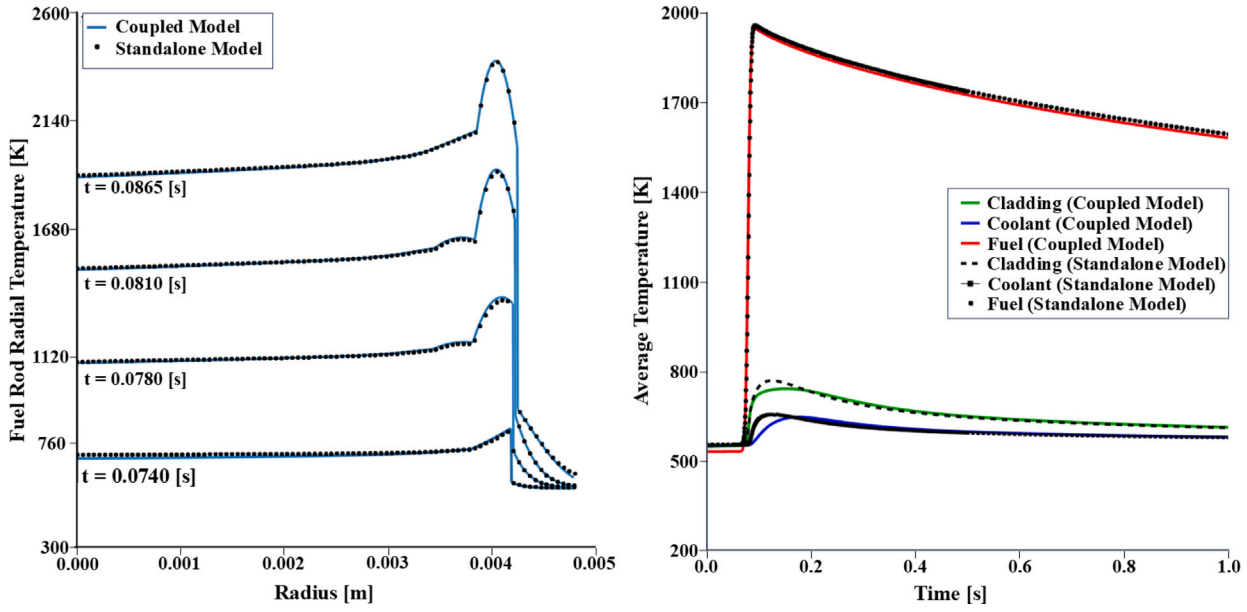

Fig. 6. Fuel rod radial temperature for different times (left) and average temperature temporal evolution (right).

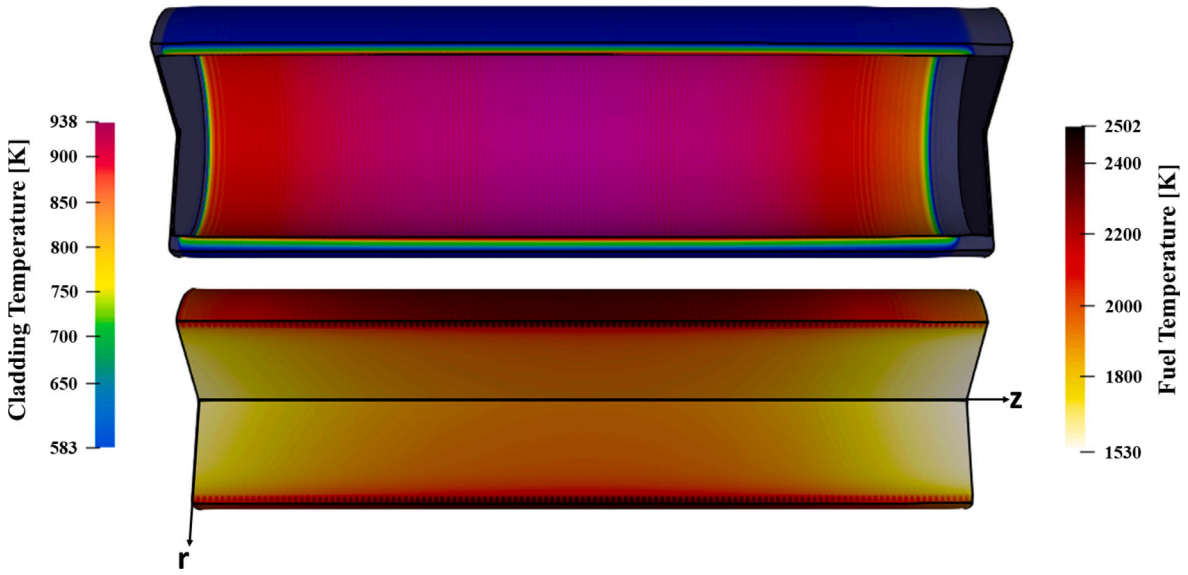

Fig. 7. Fuel and cladding temperature distribution for the timestep immediately before we reach CHF.

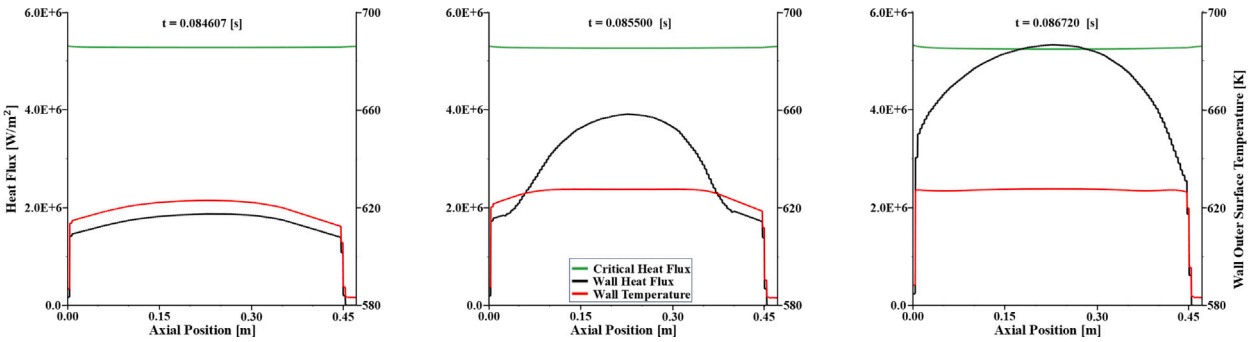

Fig. 8. Wall temperature and heat flux during the RIA for different flow regimes: subcooled (left), subcooled boiling (center), and the onset of film boiling (right).

surface temperature; a similar behavior can be seen in Fig. 10(d) with respect to the average coolant temperature.

The total energy deposition and the coolant inlet temperature also presented a slight trend toward the failure typer determination. High values of energy deposition acted in favor of PCMI failures. Increasing the total energy deposition for a fixed pulse width will reduce the time our system has to remove the energy deposited into the fuel, causing it to expand faster and favoring PCMI occurrence. For the coolant inlet temperature, lower values of this uncertainty favor the PCMI occurence. A lower inlet temperature means a higher level of subcooling in our coolant, which acts against the CHF occurrence, favoring, as a consequence, the PCMI failure occurrence.

The pitch-to-diameter ratio and the coolant mass flux did not present any noticeable trend in favor of one of the failure types. These behaviors are corroborated by the first-order Sobol indices for our system failure type, presented in Table 4, where the values inside parenthesis indicate the 95% confidence level range. We can see that the hydride rim thickness has the biggest Sobol index, indicating that the variance of this uncertainty is the main source of variance in our system failure type. The second biggest index is the power pulse width, followed by the inlet temperature and the total energy deposition, as indicated in Fig. 9.

Fig. 10 presents the temporal evolution of a few parameters for four selected cases, two for each failure type. We used two values of hydride rim thickness and two values of FWHM, while the other uncertainty values were the same between the cases. These plots help us shed light on our system's temporal evolution, focusing on variation in the two parameters with the most impact on the failure type determination. Table 5 shows the parameters used in each of these cases, as well as the failure type they undergo.

In addition to the Nantes criterion, we also conducted an analysis using the Clifford failure criterion, which is based on fuel enthalpy variation and c. This second analysis involved 44,800 model evaluations, with approximately 79.67% of them resulting in a PCMI failure. It is worth to mention that the hydride rim thickness is related to the cladding average hydride concentration through Eq. (11). The Clifford model is known for its conservative nature, which accounts for the significant increase in PCMI occurrences when transitioning from one model to the other.

Fig. 11 presents the results for the Clifford criterion case. As we can see, the hydride rim thickness, directly related to the cladding average hydride content, has a huge impact on the failure type determination but now covers a much broader region than the over-covered by the Nantes criterion. Narrow power pulse widths also favored the occurrence of PCMI failures since they led the fuel enthalpy to rise quickly, not giving time to our system undergoing a CHF failure.

Overall, the trends presented by the uncertainties in the Nantes failure criterion in Fig. 9 were preserved when compared against the Clifford model. From Fig. 11, we can also see how the inlet coolant temperature and the total energy deposition also contribute to the variance in our system failure type determination. In the same way, the pitch-to-diameter ratio and mass flux did not present any remarkable trend, indicating that for both models, these quantities have a small capacity to influence the type of failure our system will suffer when compared to the other uncertainties considered in this study.

Table 4
First- and second-order Sobol indices for our system failure type.

S_i (95%)	E_d	$FWHM$	T_{inlet}	G	P/D	δ_{Rim}
E_d	0.00772 (0.00617, 0.00927)	0.00104 (−0.00184, 0.00393)	0.00093 (−0.00160, 0.00347)	0.00000 (−0.00253, 0.00253)	0.00012 (−0.00245, 0.00270)	0.01261 (0.00912, 0.01610)
$FWHM$	———	0.11235 (0.10612, 0.11858)	0.00012 (−0.00893, 0.00916)	0.00002 (−0.00892, 0.00896)	0.00005 (−0.00902, 0.00912)	0.21485 (0.20067, 0.22903)
T_{inlet}	———	———	0.01360 (0.01164, 0.01556)	0.00035 (−0.00264, 0.00334)	0.00017 (−0.00285, 0.00319)	0.02775 (0.02354, 0.03195)
G	———	———	———	0.00103 (0.00038, 0.00168)	0.00006 (−0.00090, 0.00103)	0.00170 (0.00046, 0.00295)
P/D	———	———	———	———	0.00327 (0.00210, 0.00444)	0.00653 (0.00410, 0.00895)
δ_{Rim}	———	———	———	———	———	0.59561 (0.58541, 0.60581)

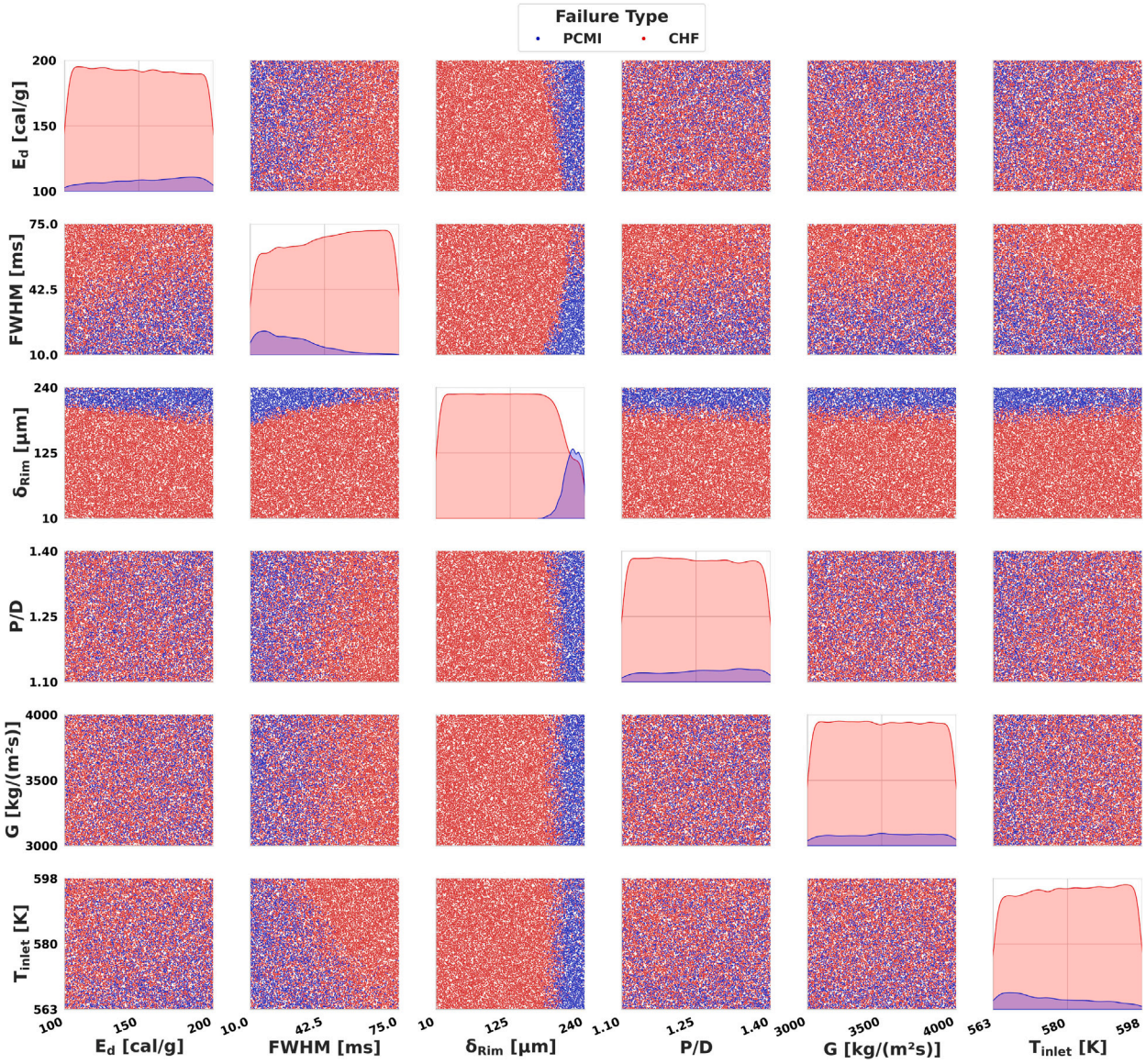

Fig. 9. Failure type as a function of the uncertainties analyzed in this study for the Nantes failure criterion.

Table 5
Uncertainty values used for each case presented in Fig. 10.

	FWHM [ms]	δ_{Rim} [μm]	E_d [cal/g]	P/D	G kg/(m^{2}s)	T_{inlet} [K]	Failure time [s]	Failure type
Case 1	10.00788	97.24076	176.68391	1.2307	3118.02173	563.80968	0.03472	CHF
Case 2	10.00788	209.03367	176.68391	1.2307	3118.02173	563.80968	0.02561	PCMI
Case 3	42.59989	97.24076	176.68391	1.2307	3118.02173	563.80968	0.11224	CHF
Case 4	42.59989	209.03367	176.68391	1.2307	3118.02173	563.80968	0.11028	PCMI

Fig. 12 shows the isolated result from Figs. 9 and 11 for the failure type as a function of the hydride rim thickness and the power pulse FWHM where we can see more clearly the boundary between the PCMI and CHF failures. These boundaries can be expressed as a polynomial equation correlating the hydride rim thickness to the power pulse FWHM, with the form:

$$FWHM_{Boundary} = a * \delta_{Rim}^3 + b * \delta_{Rim}^2 + c * \delta_{Rim} + d \quad (22)$$

where the coefficients for Eq. (22) are presented in Table 6.

Table 6
Eq. (22) coefficients.

	a	b	c	d
Nantes	0.0000000000	0.0151180035	−4.6818577805	370.4253517974
Clifford	0.0002892901	−0.0555349053	4.1585376708	−71.6480193510

5. Conclusion

This work presented the development of a MOOSE-based computational model to study the behavior of a fuel rod during the first

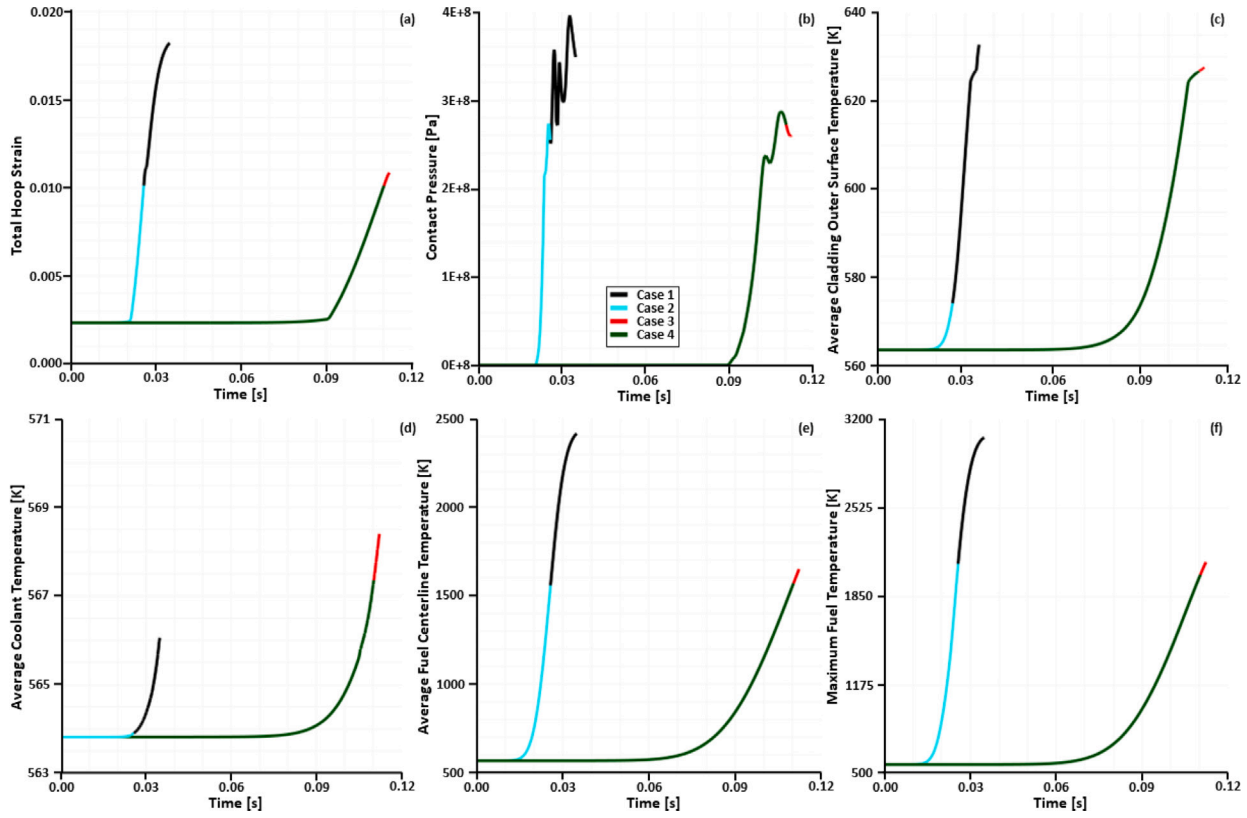

Fig. 10. Total hoop strain (a), contact pressure (b), average cladding outer surface temperature (c), average coolant temperature (d), average fuel centerline temperature (e), and maximum fuel temperature as a function of time for the four cases described in Table 5.

stages of an RIA transient for high-burnup fuels. We performed 145,600 simulations divided into two groups to address how the pulse total energy deposition, E_d, pulse FWHM, the hydride rim thickness, δ_{Rim}, the pitch-to-diameter ratio, P/D, and the coolant mass flux, G, and inlet temperature T_{inlet} would impact the fuel rod's failure during the RIA for two types of PCMI failure criterion, with the Nantes criterion indicating around 8.16% of PCMI failures. In contrast, the fuel enthalpy-based criterion suggested that 79.67% of the failures happened due to PCMI. These results highlight that RIA failure criteria based on the fuel enthalpy variation during the RIA will highly overestimate the PCMI occurrence.

We validated our MOOSE-THM/BISON REP-Na3 model against some of the available experimental data for this test. The computational model fairly agreed with the experimental data as shown through Fig. 5 and Table 3. We also performed a code-to-code benchmark between our model and a BISON standalone model to ensure that the solid domain of our model, which we do not have experimental data to compare, behaves as expected. This result was presented in Fig. 6. For the cases we ran using water as the coolant, the lack of available experimental data prevented us from performing model validation.

For the PWR operational conditions, the wall temperature and heat flux are consistent with the behavior described in the literature, where once the subcooled boiling regime is reached, the enhancement in the heat removal rate caused by the phase transition and the bubbles departure from the clad surface makes the rise in the clad temperature to slow down, giving to the axial temperature distribution a characteristic flat profile that can be seen in Fig. 8, indicating that our model is capable of identifying three operational scenarios: subcooled flow, subcooled boiling flow, and the onset of film boiling that follows the system reaching the critical heat flux. Our computational model also successfully characterized two failure scenarios: high-temperature failures in which the cladding reached CHF and low-temperature failures in which the clad failed due to PCMI.

Our results suggest that the hydride rim thickness and the power pulse width during the RIA will be the main factors in determining what type of failure our system would suffer during the power t ansient. The impact of these parameters on our system failure type determination is clear if we look at the distribution of failures presented in Fig. 9 and how each uncertainty contributed to determining how our system would fail. It also indicates that the pitch-to-diameter ratio and the coolant mass flux will have a minor impact on the determination of our system failure type in comparison to the other uncertainties considered. These findings were further corroborated by the distribution of the Sobol index over the parameters used in the sensitivity analysis. The Sobol indices are presented in Table 4.

Our comparison between the Nantes PCMI failure criterion against the Clifford PCMI failure criterion for RIA indicates that even overestimating the PCMI occurrence, the results where the Clifford criterion was used followed the same trend as the ones were we used the Nantes criterion, highlighting the Clifford criterion conservative behavior.

Our results also suggest that experiments that intend to undergo PCMI failures during RIAs would have a better chance of capturing the phenomenon if they used claddings with a significant hydride rim structure subjected to narrow power pulses and a higher coolant subcooled level. Fig. 9 also intends to act as a guide to help in the design of future RIA experiments for PWRs based on the type of failure to be analyzed. We providede polynomial functions for the boundary between PCMI and CHF failures as a function of the hhydride rim thickness and pulse FWHM, show in Fig. 12. These plots are intended to help in the determination of failure type if the hydride rim thickness and FWHM and known.

Furthermore, effects that can affect the cladding integrity, such as the hydride blister formation, which was not considered in this work, will also influence how our system would fail. In future work, accounting for these effects will help to improve our current analysis, allowing us to elaborate more precise failure maps and have a better

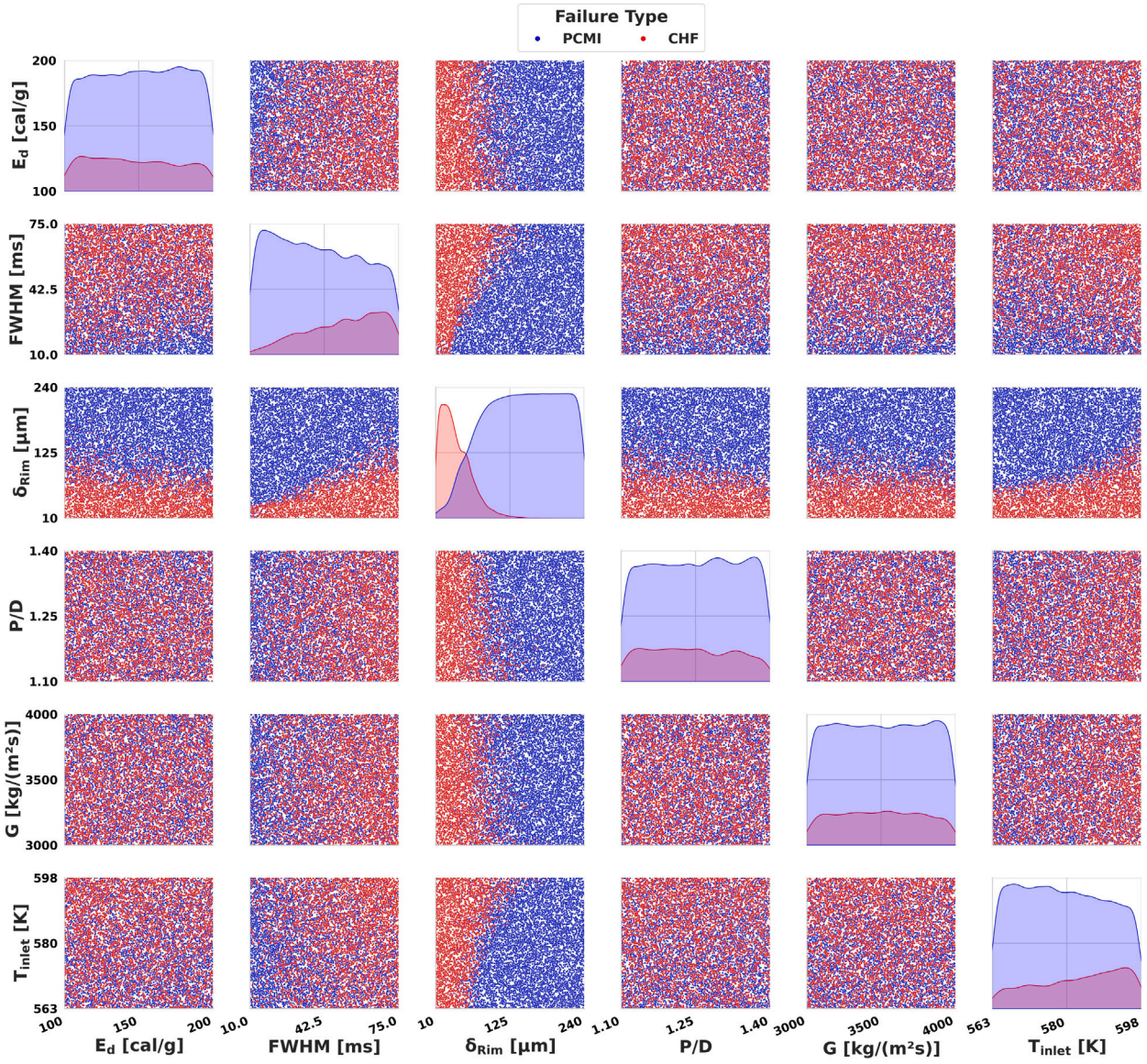

Fig. 11. Failure type as a function of the uncertainties analyzed in this study for Clifford failure criterion.

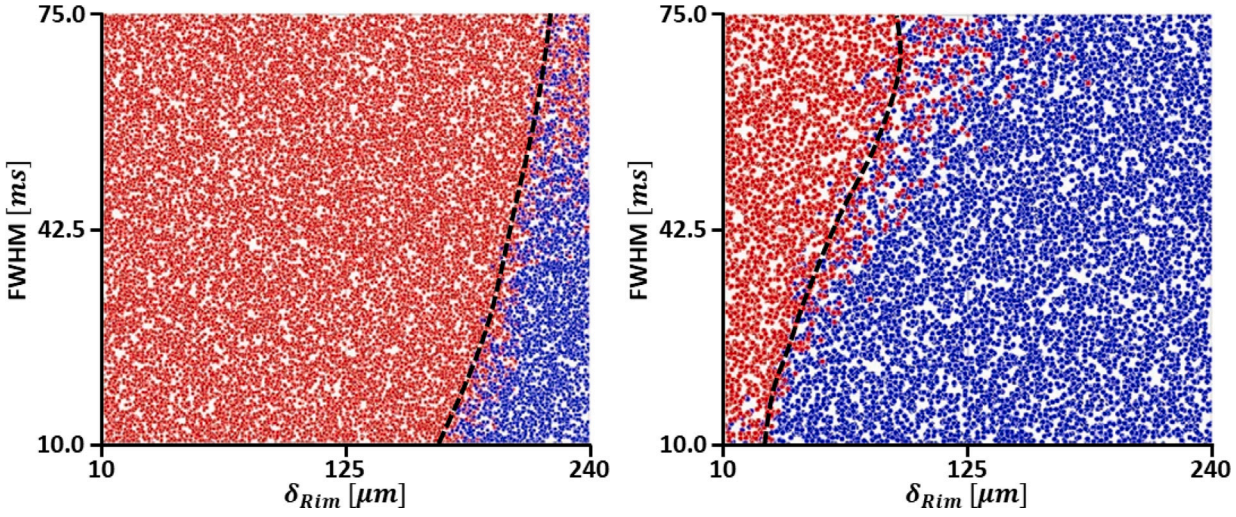

Fig. 12. Boundary between PCMI and CHF failures for the Nantes (left) and Clifford (right) PCMI failure criterion.

understanding of the fuel rod evolution during the first stages of an RIA transient.

CRediT authorship contribution statement

L. Aldeia Machado: Writing – original draft, Software, Methodology, Investigation, Conceptualization. **K. Nantes:** Methodology, Writing – review & editing. **E. Merzari:** Writing – review & editing, Supervision, Project administration, Methodology, Investigation, Funding acquisition, Conceptualization. **L. Charlot:** Writing – review & editing, Supervision, Methodology, Investigation, Conceptualization. **A. Motta:** Writing – review & editing, Supervision, Project administration, Methodology, Investigation, Funding acquisition, Conceptualization. **W. Walters:** Supervision, Conceptualization.

Declaration of competing interest

The authors declare the following financial interests/personal relationships which may be considered as potential competing interests: Luiz Carlos Aldeia Machado reports financial support was provided by US Department of Energy. Luiz Carlos Aldeia Machado reports equipment, drugs, or supplies was provided by Idaho National Laboratory. If there are other authors, they declare that they have no known competing financial interests or personal relationships that could have appeared to influence the work reported in this paper.

Acknowledgments

This material is based upon work supported by a Department of Energy Nuclear Energy University Programs Graduate Fellowship.

This research used the resources of the High-Performance Computing Center at Idaho National Laboratory, which is supported by the Office of Nuclear Energy of the U.S. Department of Energy and the Nuclear Science User Facilities under Contract No. DE-AC07-05ID14517.

Data availability

Data will be made available on request.

References

Bates, D.W., 1998. Influence of Stress State and Hydrogen on Deformation and Failure of Zircaloy-4 (Ph.D. thesis). Pennsylvania State University.

Berry, R.A., Zou, L., Zhao, H., Zhang, H., Peterson, J.W., C., M.R., Kadioglu, D., Andrs, D., 2014. RELAP-7 theory manual.

Beyer, C.E., Geelhood, K.J., 2013. Pellet-Cladding Mechanical Interaction Failure Threshold for Reactivity Initiated Accidents for Pressurized Water Reactors and Boiling Water Reactors. Technical Report, Pacific Northwest National Lab. (PNNL), Richland, WA (United States).

Biard, B., Chevalier, V., Gaillard, C., Georgenthum, V., Grando, Q., Guillot, J., Lebreton, L., Manenc, C., Mirotta, S., Monchalin, N., 2020. Reactivity initiated accident transient testing on irradiated fuel rods in PWR conditions: The CABRI international program. Ann. Nucl. Energy 141, 107253.

Boyack, B.E., Motta, A.T., Peddicord, K.L., Alexander, C.A., Deveney, R.C., Dunn, B.M., Fuketa, T., Higar, K.E., Hochreiter, L.E., Jensen, S.E., et al., 2001. Phenomena identification and ranking tables (PIRTs) for reactivity initiated accidents in pressurized water reactors containing high burnup fuel. Nucl. Regul. Comm. NUREG/CR 6742.

Clifford, P., 2020. Pressurized-Water Reactor Control Rod Ejection and Boiling-Water Reactor Control Rod Drop Accidents. Technical Report Regulatory Guide RG 1.236, United States Nuclear Regulatory Commission, pp. 1–29.

Daum, R.S., 2007. Hydride-Induced Embrittlement of Zircaloy-4 Cladding Under Plane-Strain Tension. The Pennsylvania State University.

EPRI, 2004. Fuel analysis and licensing code: FALCON MOD01 - volume 3: Verification and validation. (1011309).

Folsom, C.P., Williamson, R.L., Pastore, G., Liu, W., 2017. Development of a RIA experimental benchmark for BISON.

Fuketa, T., Nagase, F., Ishijima, K., Fujishiro, T., 1996. NSRR/RIA experiments with high-burnup PWR fuels. Nucl. Saf. 37 (4), 328–342.

Groeneveld, D.C., 2019. Critical Heat Flux Data used to Generate the 2006 Groeneveld Lookup Tables. Technical Report, United States Nuclear Regulatory Commission.

Groeneveld, D.C., Shan, J.Q., Vasić, A.Z., Leung, L.K.H., Durmayaz, A., Yang, J., Cheng, S.C., Tanase, A., 2007. The 2006 CHF look-up table. Nucl. Eng. Des. 237 (15), 1909–1922, NURETH-11.

Hales, J.D., Gamble, K.A., Spencer, B.W., Novascone, S.R., Pastore, G., Liu, W., Stafford, D.S., Williamson, R.L., Perez, D.M., Gardner, R.J., 2015. BISON users manual.

Hansel, J., Andrs, D., Charlot, L., Giudicelli, G., 2024. The MOOSE thermal hydraulics module. J. Open Source Softw. 9 (94), 6146.

Hernandez, R., Armstrong, R.J., Seo, S.B., Folsom, C.P., Jensen, C.B., Brown, N.R., 2022. Sensitivity analysis of in-pile CHF experiments in the TREAT facility: Characterization of impacts of fuel system thermal properties. Ann. Nucl. Energy 165, 108645.

Kamerman, D.W., Jensen, C.B., Wachs, D.M., Woolstenhulme, N.E., 2022. High-Burnup Experiments in Reactivity Initiated Accidents (HERA). Technical Report, Idaho National Lab. (INL), Idaho Falls, ID (United States).

Link, T.M., 1997. Failure of Zircaloy Cladding under Severe Loading Conditions (Ph.D. thesis). Pennsylvania State University.

Marion, A., 2006. Safety evaluation by the office of nuclear reactor regulation of electric power research institute (EPRI) topical report TR-1002865, "Topical report on reactivity initiated accidents: Bases for RIA fuel rod failures and core coolability criteria. http://pbadupws.nrc.gov/docs/ML0616/ML061650107.pdf.

Métayer, O.L., Massoni, J., Saurel, R., 2004. Elaborating equations of state of a liquid and its vapor for two-phase flow models. Int. J. Therm. Sci. 43, 265–276.

Meyer, R.O., Scott, H.H., McCardell, R.K., 1996. Regulatory assessment of test data for reactivity-initiated accidents. Nucl. Saf. 37 (4).

Nantes, K.R.B., Jin, M., Motta, A.T., 2024a. Hydrided zircaloy-4 cladding failure criteria during reactivity-initiated accidents. In: Proceedings of the 2024 ANS Annual Meeting. ANS.

Nantes, K.R.B., Jin, M., Motta, A.T., 2024b. Modeling hydrogen localization in zircaloy cladding subjected to temperature gradients. J. Nucl. Mater. 589, 154853.

Papin, J., Balourdet, M., Lemoine, F., Lamare, F., Frizonnet, J.M., Schmitz, F., 1996. French studies on high-burnup fuel transient behavior under RIA conditions. Nucl. Saf. 37 (4), 289–327.

Papin, J., Cazalis, B., Frizonnet, J.M., Desquines, J., Lemoine, F., Georgenthum, V., Lamare, F., Petit, M., 2007. Summary and interpretation of the CABRI REP-Na program. Nucl. Technol. 157 (3), 230–250.

Papin, J., Petit, M., Grandjean, C., Georgenthum, V., et al., 2006. IRSN R&D studies on high burnup fuel behaviour under RIA and loca conditions. In: Proceedings of the 2006 International Meeting on LWR Fuel Performance. pp. 274–278.

Recuero, A., Lindsay, A., Yushu, D., Peterson, J.W., Spencer, B., 2022. A mortar thermomechanical contact computational framework for nuclear fuel performance simulation. Nucl. Eng. Des. 394, 111808.

Schmitz, F., Papin, J., 1999. High burnup effects on fuel behavior under accident conditions: The tests CABRI REP-Na. J. Nucl. Mater. 270 (1–2), 55–64.

Seo, S.B., Armstrong, R.J., Hernandez, R., Folsom, C.P., Jensen, C.B., Brown, N.R., 2021. Sensitivity analysis of in-pile critical heat flux experiments in TREAT for characterization of RIA power-transient effects. Ann. Nucl. Energy 161, 108448.

Slaughter, A.E., Prince, Z.M., German, P., Halvic, I., Jiang, W., Spencer, B.W., Dhulipala, S.L.N., Gaston, D.R., 2023. MOOSE stochastic tools: A module for performing parallel, memory-efficient in situ stochastic simulations. SoftwareX 22, 101345.

Todreas, N.E., Kazimi, M.S., 2012. Nuclear Systems: Thermal Hydraulic Fundamentals, Second Edition. Taylor & Francis.

Williamson, R.L., Hales, J.D., Novascone, S.R., Pastore, G., Gamble, K.A., Spencer, B.W., Jiang, W., Pitts, S.A., Casagranda, A., Schwen, D., Zabriskie, A.X., Toptan, A., Gardner, R., Matthews, C., Liu, W., Chen, H., 2021. BISON: A flexible code for advanced simulation of the performance of multiple nuclear fuel forms. Nucl. Technol. 207 (7), 954–980.